

Universal Fabrication of Two-Dimensional Electron Systems in Functional Oxides

Tobias Chris Rödel,^{1,2} Franck Fortuna,¹ Shamashis Sengupta,³ Emmanouil Frantzeskakis,¹ Patrick Le Fèvre,² François Bertran,² Bernard Mercey,⁴ Sylvia Matzen,⁵ Guillaume Agnus,⁵ Thomas Maroutian,⁵ Philippe Lecoer,⁵ and Andrés Felipe Santander-Syro^{1,*}

¹*CSNSM, Univ. Paris-Sud, CNRS/IN2P3,
Université Paris-Saclay, 91405 Orsay, France*

²*Synchrotron SOLEIL, L'Orme des Merisiers,
Saint-Aubin-BP48, 91192 Gif-sur-Yvette, France*

³*Laboratoire de Physique des Solides, Univ. Paris-Sud,
CNRS, Université Paris-Saclay, 91405 Orsay, France*

⁴*CRISMAT, ENSICAEN-CNRS UMR6508,
6 bd. Maréchal Juin, 14050 Caen, France*

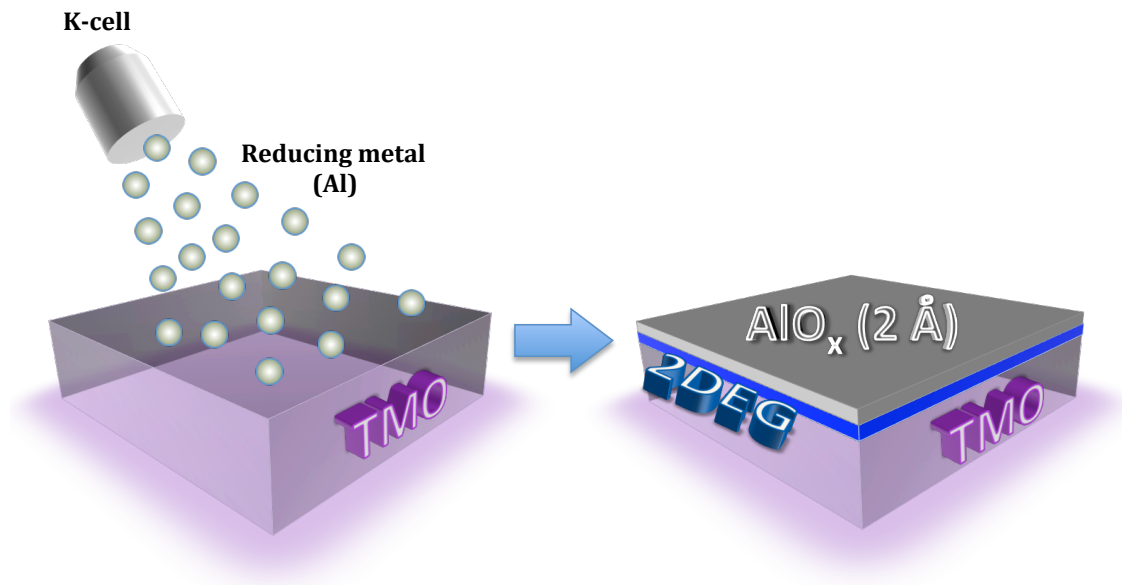
⁵*Institut d'Electronique Fondamentale, Univ. Paris-Sud,
CNRS, Université Paris-Saclay, 91405 Orsay, France*

This is the peer reviewed version of the following article: T. C. Rödel, F. Fortuna, S. Sengupta, E. Frantzeskakis, P. Le Fèvre, F. Bertran, B. Mercey, S. Matzen, G. Agnus, T. Maroutian, P. Lecoer, and A. F. Santander-Syro. *Universal fabrication of 2D electron systems in functional oxides*. Adv. Mater. **28**, 1976-1980 (2016), which has been published in final form at <https://doi.org/10.1002/adma.201505021>. This article may be used for non-commercial purposes in accordance with Wiley Terms and Conditions for Use of Self-Archived Versions.

Table of contents entry

Two-dimensional electron systems (2DESs) in functional oxides are promising for applications, but their fabrication and use, essentially limited to SrTiO₃-based heterostructures, are hampered by the need of growing complex oxide over-layers thicker than 2 nm using evolved techniques. This work shows that thermal deposition of a monolayer of an elementary reducing agent suffices to create 2DESs in numerous oxides.

Keyword: 2DES in oxide surfaces and interfaces.



A critical challenge of modern materials science is to tailor novel states of matter suitable for future applications beyond semiconductor technology. Two-dimensional electron systems (2DESs) in multi-functional oxides [1] can show metal-to-insulator transitions [2], superconductivity [3, 4], magnetism [5–7], or spin-polarized states [8–10], and are thus an active field of current research [11–13]. However, the fabrication of 2DESs in oxide heterostructures, like $\text{LaAlO}_3/\text{SrTiO}_3$, requires growing a layer of binary (*e.g.* Al_2O_3) or ternary (*e.g.* LaAlO_3) oxides with a “critical thickness” of at least 20 Å using evolved deposition techniques, such as pulsed laser deposition [1, 11–17]. Thus, the reproducibility of their properties depends crucially on the growth parameters, while their fabrication is complex, expensive, and unsuitable for mass production. Moreover, the existence of a critical thickness of 20 Å for the onset of conductivity severely limits the control of the 2DES’s properties, hampering tunneling spectroscopy studies or applications that rely on charge or spin injection [18]. Similarly, the realization of 2DESs at the surface of SrTiO_3 or other oxides requires the use of intense UV or X-ray synchrotron radiation, to desorb oxygen from the surface [19–26]. Thus, these 2DESs can be only manipulated and studied in ultra-high vacuum (UHV), to preserve the vacancies from re-oxidation, and are obviously not suited for experiments or applications at ambient conditions.

Here we demonstrate a new, wholly general, extremely simple and cost-effective method to generate 2DESs in functional oxides. We use thermal evaporation from a Knudsen cell to deposit, at room temperature in UHV, an atomically-thin layer of an elementary reducing agent, such as pure aluminum, on the oxide surface. Due to an efficient redox reaction, the Al film pumps oxygen from the substrate, oxidizes into insulating AlO_x , and forms a pristine, homogeneous 2DES in the first atomic planes of the underlying oxide. The principle of redox reactions induced by metals at the surface of oxides is well documented [27, 28]. However, the simple idea of using a pure, elementary reducing agent to create a 2DES at a metal-oxide interface was not explored so far. This overcomes the complexity of growing an oxide thin film, the requirement of a critical thickness of insulating capping layer to create the 2DES in UHV, and the necessity, in the case of surfaces, of strong synchrotron radiation to desorb oxygen. As a novel application, we extend this method to generate a 2D metallic state at the surface of the room-temperature ferroelectric BaTiO_3 . Such hitherto unobserved coexistence of ferroelectricity and 2D conductivity in the same material is promising for functional devices using ferroelectric resistive switching [29, 30]. This new,

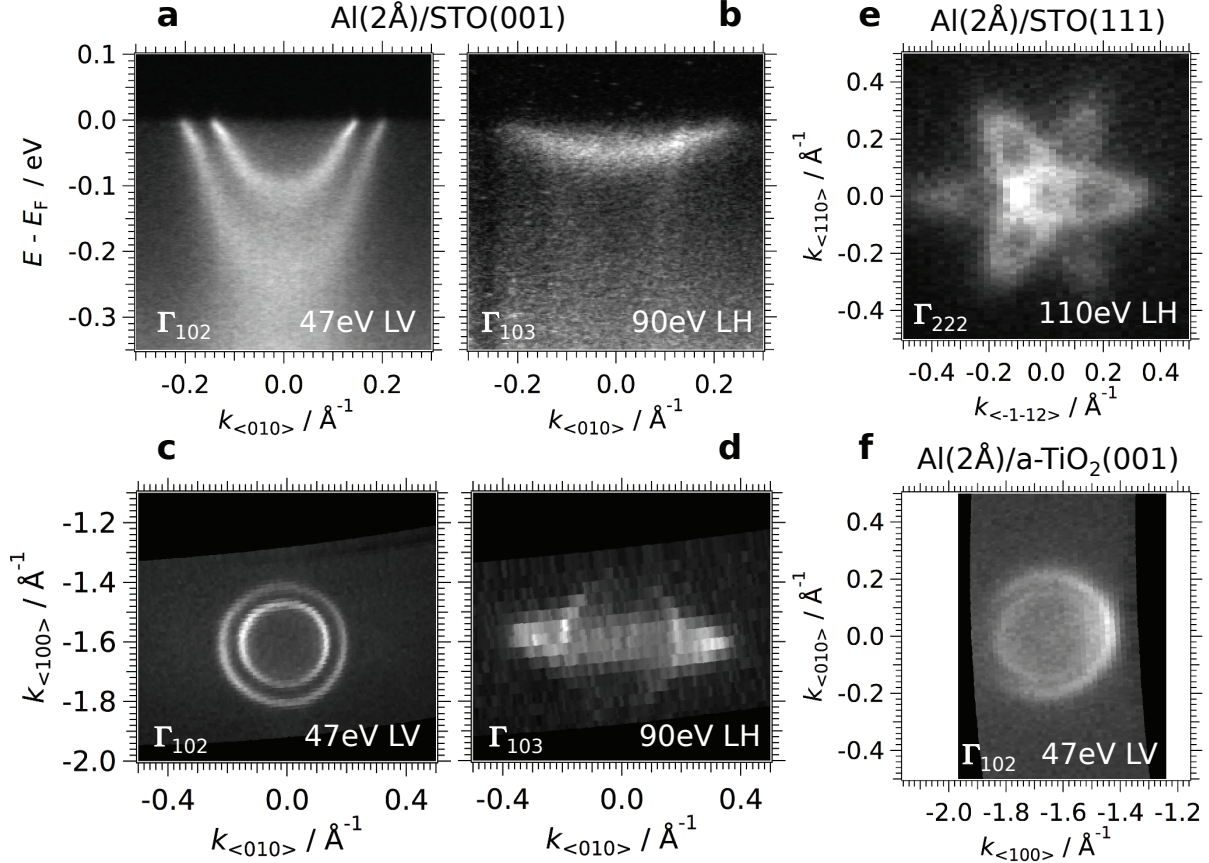


FIG. 1. (a, b) ARPES energy-momentum intensity maps measured at the Al(2Å)/SrTiO₃(001) interface prepared *in-situ*, using respectively 47 eV linear vertical (LV) and 90 eV linear horizontal (LH) photons. (c, d) Corresponding Fermi surface maps. Data at $h\nu = 47$ eV were measured around the Γ_{102} point, while data at $h\nu = 90$ eV were measured around Γ_{103} . (e, f) Fermi surface maps measured at the Al/SrTiO₃(111) and Al/TiO₂(001) anatase interfaces prepared *in-situ*. Unless specified otherwise, all spectra in this and remaining figures were measured at $T = 8$ K.

simpler and cheaper, fabrication route for 2DESs is thus adaptable to numerous oxides, given that oxygen vacancies are shallow donors in these materials, resulting in itinerant electrons. Moreover, this technique is scalable to industrial production, and ideally suited for applications that rely on charge or spin injection and for the realization of mesoscopic devices.

The existence of a 2DES at the interface between the oxidized Al layer and SrTiO₃(001), SrTiO₃(111) and anatase-TiO₂(001) is evidenced by our angle-resolved photoemission spectroscopy (ARPES) data presented in **Figure 1** –see the [Supporting Information](#) for details about the surface preparation, Al deposition, and ARPES measurements. For simplicity, and to recall that we are simply depositing pure Al (*not aluminum oxide*) on top of the

oxide surfaces, all throughout this paper we note the resulting oxidized Al capping layer simply as “Al”, specifying in parenthesis the evaporated thickness. The energy-momentum and Fermi surface maps formed by the t_{2g} orbitals, shown in Figure 1, agree with previous ARPES studies at the reduced surface of these materials [19, 20, 24–26, 31], demonstrating that in both cases the same 2DESs are observed.

Note that, instead of the local creation of oxygen vacancies using an intense UV beam, the evaporated Al reduces the whole surface homogeneously. As a consequence, the data quality, evidenced by the line widths, is also much better than in previous studies. Thus, as shown in Figure 1(a), a kink and change in intensity in the dispersion of the light bands at $E \approx -30$ meV, attributed to electron-phonon coupling [32], can be very clearly distinguished.

The Fermi-surface areas and, hence, the charge carrier densities of the 2DESs at the Al/SrTiO₃(111) and Al/TiO₂(001) interfaces are about 1.3 and 2 times larger than their counterparts at the surfaces reduced by photons, probably due to a higher and more homogeneous concentration of oxygen vacancies.

To understand the redox reaction at the Al/oxide interface, we probed the oxidation state of Al by measuring the Al-2*p* core levels, whose binding energies are very different for metallic and oxidized Al. As shown in **Figure 2(a)**, the two contributions can be distinguished in the Al(6Å)/STO spectrum (blue curve), with the metallic component around 72.5 eV binding energy and the oxidized part around 75 eV binding energy. In contrast, the metallic Al component decreases for a thinner 4Å film (black curve), and the deposition of only 2Å of pure Al results in a nearly fully oxidized film of Al (red curves). In other words, *an ultra-thin layer of 2Å of pure Al is sufficient to pump the oxygen from the surface region of all the oxides studied in this work.* The spatial distribution of the oxygen vacancies close to the interface is discussed in the Supporting Information. Note that the oxidation of the metallic Al results in an increased layer thickness: as the mass density of Al is 2.7 g/cm³ and the one of amorphous Al₂O₃ is about 4 g/cm³, the deposition of 2Å of Al yields an oxidized Al film of 2.5Å.

To determine if the thickness of the Al-layer has an influence on the electron density of the 2DES, we turn to the momentum distribution curves (MDCs) at the Fermi level as shown in Figure 2(b). As can be seen in Figure 2(b), the Fermi momenta are essentially the same, within 0.01 Å⁻¹ for the 2Å (red MDC), 4Å (black) and 6Å (blue) thick Al films. As the 2D density of electrons depends solely on the Fermi momenta, it is clear that this electron

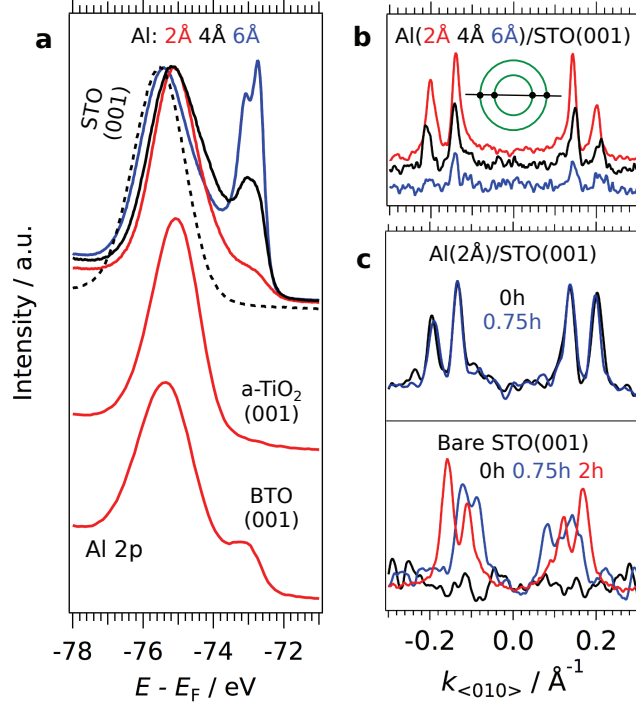


FIG. 2. (a) Angle-integrated spectra of the Al 2p peak of the Al/SrTiO₃(001) Al/TiO₂ anatase and Al/BaTiO₃(001) interfaces measured at a photon energy of $h\nu = 100$ eV. The curves in different colors correspond to different thicknesses of Al (red 2Å, black 4Å, blue 6Å). The peak shape of the Al 2p peak indicates if the Al layer is oxidized or metallic. The dashed black curve corresponds to a fully oxidized Al layer, obtained after annealing the sample with 4 Å Al capping at 250°C in UHV. (b) Momentum distribution curves (MDCs) at E_F , along the Fermi-surface cut schematized in the inset, measured at the Al/SrTiO₃(001) interface at $h\nu = 47$ eV for different Al thicknesses. Peaks in the MDCs correspond to the Fermi momenta, where the MDC cuts the Fermi surface. The decrease in intensity of the MDCs for increasing Al thickness is merely due to increasing damping of the photoemission signal. (c) MDCs integrated over $E_F \pm 5$ meV for increasing UV exposure times on the Al/SrTiO₃(001) interface and the bare STO surface measured under identical conditions. The similarity of the two MDCs at the interface is in strong contrast to the evolution under light irradiation of the MDCs at the bare surface.

density already saturates at an Al film thickness of 2Å. Thus, our method overcomes the necessity of a “critical thickness” of capping layer to generate a 2DES in UHV.

Previous studies on the bare surface of SrTiO₃ prepared *in-situ* showed that synchrotron UV-irradiation was necessary to create the oxygen vacancies responsible for the 2DES [20, 25, 26, 31]. This is again demonstrated in the lower panel of Figure 2(c), which shows the evolution with time of the MDC at E_F upon UV-irradiation on a bare SrTiO₃(001) surface. While the 2DES is absent at $t = 0$ h (black MDC), its carrier density increases up to saturation upon UV irradiation (blue and red MDCs), as denoted by the increase of k_F

for increasing exposure times.

Contrary to the bare surface, there is *no measurable influence* of the UV irradiation on the electronic structure of the Al/SrTiO₃ system, neither on the charge carrier density nor on the line-shapes or spectral weight of the 2DES, as demonstrated in the top panel of Figure 2(c): the MDCs at E_F show a stable subband structure and a maximum electron density from the very beginning of the measurements. This indicates that the oxygen vacancy concentration and distribution, due the redox reaction at the interface between Al and SrTiO₃, is already saturated and stable upon irradiation.

As demonstrated in the [Supporting Information](#), the 2DES at the interface of oxidized Al/SrTiO₃ is stable also at room temperature, while the deposition of an Al film of 10Å or more on SrTiO₃ minimizes the re-oxidation of vacancies in air.

We now show that the deposition of an ultra-thin Al film can also be used to create a 2DES at the surface of the room-temperature ferroelectric BaTiO₃ (BTO), thus constituting a new type of confined metallic state on a truly room-temperature functional oxide. Our BTO samples are (001)-oriented thin films (thickness 30 nm) epitaxially grown on SrTiO₃(001) –see [Supporting Information](#) for details about thin-film growth, piezo-response force microscopy (PFM), and capacitance-voltage (C-V) measurements. In contrast to the bulk crystals, which usually exhibit ferroelectric-domain stripes of period $\sim 50 - 200$ nm, even down to 100 nm scale thicknesses [33], the 30 nm-thick BTO films deposited on Nb:STO show a single domain state, with the ferroelectric polarization aligned along the [001] axis, due to the in-plane compressive strain induced by the epitaxial growth [34–36].

The absence of ferroelectric domains and the local reversibility of the polarization are demonstrated in **Figures 3(a, b)** by the simultaneous atomic force microscopy (AFM) and PFM images of a BaTiO₃/Nb:SrTiO₃ thin film.

The energy-momentum ARPES intensity maps of Figures 3(c-e) prove the formation of metallic itinerant states at the surface of the BTO(001) thin-film after deposition of 2 Å of Al. The resulting 2DES is constituted of a light (d_{xy} -like) and a heavy ($d_{xz/yz}$ -like) electron pocket around Γ , best observed in Figures 3(c, d) with LV and LH polarizations, respectively. Such light-polarization-dependent selection rules are typical for t_{2g} -like states observed at the surface of other titanates, such as SrTiO₃ and anatase [19, 26]. In the case of BaTiO₃, the light band forms a strong peak of spectral weight whose intensity is cut-off at E_F –see Figure 3(c). Although we cannot observe a dispersive feature within this peak

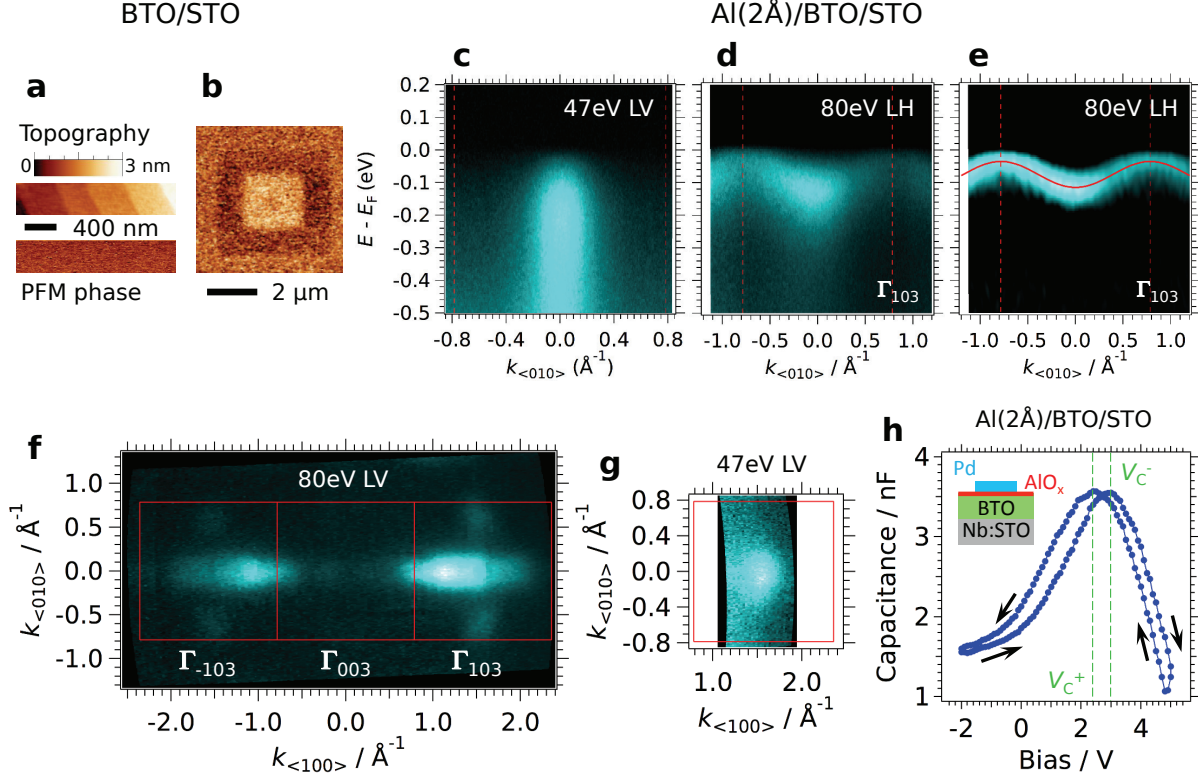


FIG. 3. (a) AFM topography and corresponding PFM phase signal measured on a 30 nm-thick BaTiO₃/Nb:SrTiO₃ film. No ferroelectric domains could be detected in the as-grown film, while such domains can be written, as shown in (b), with +6 V on the AFM tip in the outer square ($4 \times 4 \mu\text{m}^2$) and -6 V in the inner square ($2 \times 2 \mu\text{m}^2$). (c, d) ARPES energy-momentum intensity maps at the Al(2Å)/BaTiO₃ interface prepared *in-situ*, using respectively 47 eV LV and 80 eV LH photons, the latter being close to Γ_{103} . (e) Second energy-derivative (negative values) of the ARPES map in (d). Vertical dashed red lines in (c)-(e) are the Brillouin-zone edges. The red curve in (e) is a cosine fit to the heavy band. (f, g) Spectral weight integrated over $E_F \pm 30$ meV at the Al(2Å)/BaTiO₃ interface using 80 eV LV and 47 eV LV photons, respectively. (h) Capacitance-voltage curve on the Al(2Å)/BaTiO₃ interface measured previously by ARPES, showing the butterfly shape characteristic of a ferroelectric hysteresis. A Pd circular pad and the Nb:STO substrate were used as top and bottom electrodes, respectively. Note that, due to the voltage drop through the thin alumina layer, the voltages V_c^+ and V_c^- required to reverse the polarization are rather high. Thus, it was not possible to perform a polarization reversal in PFM mode.

of intensity, its binding energy indicates that the conduction band bottom is filled up with itinerant electrons. The heavy band, on the other hand, presents a clear dispersion –see Figures 3(d, e). A tight-binding fit of this band, red curve in Figure 3(e), yields a band bottom of -115 meV at Γ , a band top of -35 meV at the zone edge, and an effective mass near Γ of approximately $12m_e$.

Figures 3(f, g) show that the spectral weight at E_F is composed of a central disc formed by

the light electron pocket, best seen in Figure 3(g), and two orthogonal Fermi-surface strips spanning the entire Brillouin zone, formed by the heavy bands. These last correspond to the elliptical Fermi sheets observed at the surface of SrTiO₃(001), as in Figure 1(d), but in the case of BaTiO₃(001) they extend beyond the zone boundary, thus forming open Fermi sheets. From Figure 3(g), the distribution of spectral weight at E_F for the circular Fermi surface spans a Fermi momentum $k_F \approx 0.15 \pm 0.02 \text{ \AA}^{-1}$. The Fermi strips can be approximated as rectangles of long and short sides $k_l = 2 \times \pi/a$ (with $a = 4 \text{ \AA}$ the size of the square unit cell at the BTO surface) and $k_s = 0.15 \pm 0.02 \text{ \AA}^{-1}$. From the total area A_F enclosed by all the Fermi surfaces, the density of carriers of the 2DES at the BaTiO₃(001) surface is $n_{2D}^{\text{BTO}(001)} = A_F/(2\pi^2) \approx (2.8 \pm 0.4) \times 10^{14} \text{ cm}^{-2}$, which is comparable to the density of states at the SrTiO₃ or anatase-TiO₂ surfaces. The [Supporting Information](#) presents additional data showing the Fermi momenta extracted from fits to the spectra, and the photon-energy dependence of the electronic structure.

Finally, Figure 3(h) shows a measurement of the capacitance-voltage curve on the *same* Al(2Å)/BaTiO₃ interface that was measured by ARPES. The “butterfly” shape, with a difference of about 0.5 V between the two coercive voltages, demonstrates that the BTO film is still ferroelectric after deposition of the Al layer and ARPES measurements, thus keeping its functional behavior.

A 2DES at the surface of BaTiO₃ is in essence an intrinsic metal/ferroelectric interface. Polarization switching of the bulk material, for instance by strain, could allow a direct gating of the 2DES, while a sufficiently thick capping alumina layer protects it against re-oxidation at ambient conditions, and can be even used to draw metallic nano-circuits of intrinsic ferroelectric tunnel junctions. Thus, this system provides a realistic platform for the realization of non-volatile memories using ferroelectric resistive switching [29, 30] or for ultra-sensitive strain or pressure detectors.

In conclusion, the method we present here for realizing 2DESs in oxides has the advantages of simplicity and versatility –for instance, it can be readily implemented in many UHV setups, allowing future investigations of 2DESs in complex oxides using non-synchrotron based spectroscopic techniques, like tunneling or Raman spectroscopies. This method is also pertinent for the study of transport phenomena in mesoscopic oxide devices. Indeed, STO has emerged as an exciting nano-electronics device platform [37], owing to the existence of superconductivity, spin-orbit interaction and magnetism which are controllable with a gate

voltage. Our work opens up new possibilities to explore these questions by making a class range of transition-metal oxide 2DESs suitable for transport, including the surfaces which are candidates for hosting topological electronic states [23, 24]. Furthermore, the stability of the 2DES in ambient conditions can be achieved through a sufficiently thick layer of oxidized Al. This opens the possibility to integrate TMO 2DESs into functional devices without the need of evolved deposition techniques.

Experimental Section

The ARPES measurements were conducted at the CASSIOPEE beamline of Synchrotron SOLEIL (France). We used linearly polarized photons in the energy range 30 – 110 eV and a hemispherical electron analyzer with vertical slits. The angular and energy resolutions were 0.25° and 15 meV. The mean diameter of the incident photon beam was smaller than 100 μm . The samples were cooled down to $T = 8$ K before measuring. Unless specified otherwise, all data were taken at that temperature. The results have been reproduced on more than 10 samples for $\text{SrTiO}_3(001)$, and on at least two samples for other surface orientations and for TiO_2 anatase, and on 3 thin films of $\text{BaTiO}_3/\text{SrTiO}_3(001)$. All through this paper, reciprocal-space directions $\langle hkl \rangle$ and planes (hkl) are defined in the conventional cell of each material (cubic for SrTiO_3 , simple tetragonal for anatase and BaTiO_3). The indices h , k , and l of Γ_{hkl} correspond to the reciprocal lattice vectors of the cubic unit cell (SrTiO_3 and BaTiO_3) or body-centered tetragonal unit cell (anatase).

Additional details on the sample and surface preparation, the Al deposition conditions, and the piezo-response force microscopy and capacitance-voltage measurements can be found in the [Supporting Information](#).

Acknowledgements

We thank illuminating discussions with M. Gabay and M. J. Rozenberg, and V. Pilard for help with the sample preparation. This work is supported by public grants from the French National Research Agency (ANR), project LACUNES No ANR-13-BS04-0006-01, and the “Laboratoire d’Excellence Physique Atomes Lumière Matière” (LabEx PALM project ELECTROX) overseen by the ANR as part of the “Investissements d’Avenir” pro-

gram (reference: ANR-10-LABX-0039). T. C. R. acknowledges funding from the RTRA–Triangle de la Physique (project PEGASOS). A.F.S.-S. thanks support from the Institut Universitaire de France.

SUPPORTING INFORMATION

Sample and surface preparation and Al deposition

The non-doped, polished crystals of SrTiO₃ were supplied by CrysTec GmbH, the anatase crystals by SurfaceNet GmbH. To prepare the SrTiO₃ surfaces, the samples were ultrasonically agitated in deionized water, subsequently etched in buffered HF and annealed at 950°C for three hours in oxygen flow. This results in Ti-terminated (001) or (111) surfaces with terraces of width 50 to 200 nm separated by steps, as verified by atomic-force microscopy (AFM) in contact mode (data not shown here).

The BTO 300Å-thick films were prepared by Laser-MBE using a sintered BTO target. A Kr-F excimer laser was used for the deposition. The substrate, which was etched prior to the deposition to obtain a TiO₂ terminating layer, was glued to the heater with silver paste. The growth of the film, monitored by reflection high-energy electron diffraction (RHEED), was carried out at 650 °C in 5x10⁻⁴ mbar oxygen pressure with 0.1 % ozone. RHEED oscillations were used to measure the deposited thickness. At the end of the deposition, the films were cooled down in 6x10⁻³ mbar oxygen pressure, always with 0.1% ozone.

To clean the surfaces in UHV, the SrTiO₃ samples were annealed at a temperature $T = 550 - 650$ °C for $t = 10 - 90$ min at pressures lower than $p < 2 \times 10^{-8}$ mbar. The anatase crystals were prepared by Ar⁺ sputtering ($U = 1$ kV, $t = 10$ min) and annealing cycles ($T = 550 - 600$ °C, $t = 30$ min,) similar to the procedure described by Setvin *et al.* [38]. The surface of the BaTiO₃ thin films was cleaned by annealing the samples at temperatures $T = 500 - 550$ °C for 5 – 30 min. One of the samples was Ar⁺ sputtered ($U = 500$ V, $t = 10$ min) prior to the UHV annealing, without noticeable changes in the ARPES data.

The surface quality and the possible existence of surface reconstructions was probed by low-energy electron diffraction (data not shown here). The SrTiO₃(001) and BaTiO₃(001) surfaces are unreconstructed, whereas the (111) surface shows a 3×3 reconstruction, and the anatase (001) surface shows a two-domain 1×4 reconstruction.

To create a local, high concentration of oxygen vacancies in the surface region of SrTiO₃, TiO₂ anatase, or BaTiO₃, amorphous Al-films with thicknesses between $d = 2-10$ Å were deposited on the prepared surface of the crystals. Aluminium was evaporated from a Knudsen cell using an alumina crucible. The growth rate was approximately 0.3 Å /min, corresponding to a temperature of about 925°C of the crucible. The Al-flux was calibrated prior to the evaporation using a quartz microbalance. The cleanliness of the deposit was checked by evaporating a thin Al-film on a Cu substrate where no oxidation could be detected by Auger spectroscopy. The temperature of the crystals ranged between $T = 25 - 100$ °C during the Al deposition.

Piezo-response force microscopy and capacitance-voltage measurements

For the PFM measurements, a probing signal of 2 V_{pp} at a frequency of 25 kHz was applied to a Co/Cr coated cantilever with ~ 5 N/m force constant. A lower probing signal of 0.5 V_{pp} was also used with no change on the observed phase images such as the ones shown in Figure 3(a) of the main text. In order to assess the ferroelectric character of the BTO film measured by ARPES, 300 μm-diameter Pd electrodes (200 nm thickness) were deposited through a shadow mask on top of the Al oxide (AlO_x) layer. The C-V measurements were performed using a LCR meter with a 30 mV_{pp} AC amplitude at 10 kHz, while a source-meter allowed for the DC biasing with 0.1 V steps of 500 ms duration. The C-V curve, Figure 3(h) of the main text, shows the characteristic butterfly shape of a ferroelectric material. Note that due to the ultra-thin AlO_x layer, the required voltages to reverse the polarization (V_c) are rather high and shifted towards the positive voltage side, indicating an internal upward electric field in the BTO layer. For these reasons it was not possible to achieve a polarization reversal in PFM configuration on this sample.

Homogeneity of the 2DES

Previous studies of the 2DES at the surface of SrTiO₃ were conducted on fractured [19, 20] or *in-situ* prepared surfaces [24, 31]. The fracturing process results in locally ordered surfaces [39], while the *in-situ* preparation results in an ordered surface. The fracturing process or intense UV light irradiation at low temperature (spot size $\approx 100 \times 100\mu\text{m}$)

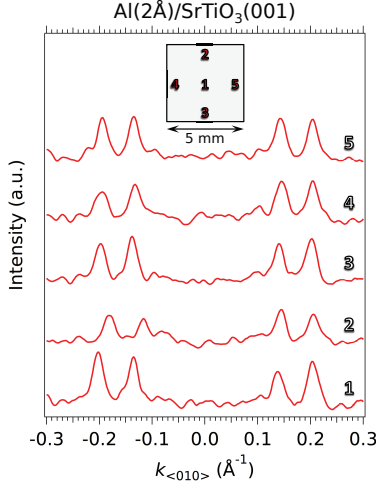


FIG. 4. (a) Momentum distribution curves integrated over $E_F \pm 5$ meV for the Al/SrTiO₃(001) interface prepared *in-situ*, measured at different positions (see inset) separated by at least 2 mm from each other -or over 100 times the size of the UV spot. Each spectrum was obtained within minutes on a part of the sample that had not been illuminated before. The Fermi momenta, given by the MDC peak positions, are independent of the position in the sample, demonstrating the homogeneity of the 2DES at the Al/SrTiO₃(001).

create a local, high concentration of oxygen vacancies in the surface region of SrTiO₃ whose electrons (partly) dope the 2DES.

In contrast to such spatial inhomogeneity of the 2DES in fractured or UV irradiated bare SrTiO₃, the fact that we cannot observe any changes induced by the synchrotron light at the Al/SrTiO₃ interface (Figure 2(c) of the main text) suggests that the underlying SrTiO₃ surface is reduced homogeneously. This is explicitly shown in **Figure 4**, which presents the momentum distribution curves at E_F measured at five different positions on the Al(2Å)/SrTiO₃ interface. We observe that the Fermi momenta, given by the MDC peaks, are independent of the measurement point, demonstrating the homogeneity of the interfacial 2DES over distances of several millimeters.

Temperature dependence of the electronic structure of the 2DES at the Al/SrTiO₃(001) interface

Figure 5(a) shows the energy-momentum maps at the Al/SrTiO₃ interface measured respectively at 21 K, 172 K, and 303 K, under the same conditions as the $E - k$ map in Figure 1(a) of the main text. The dispersions of the two light bands of d_{xy} -character are still

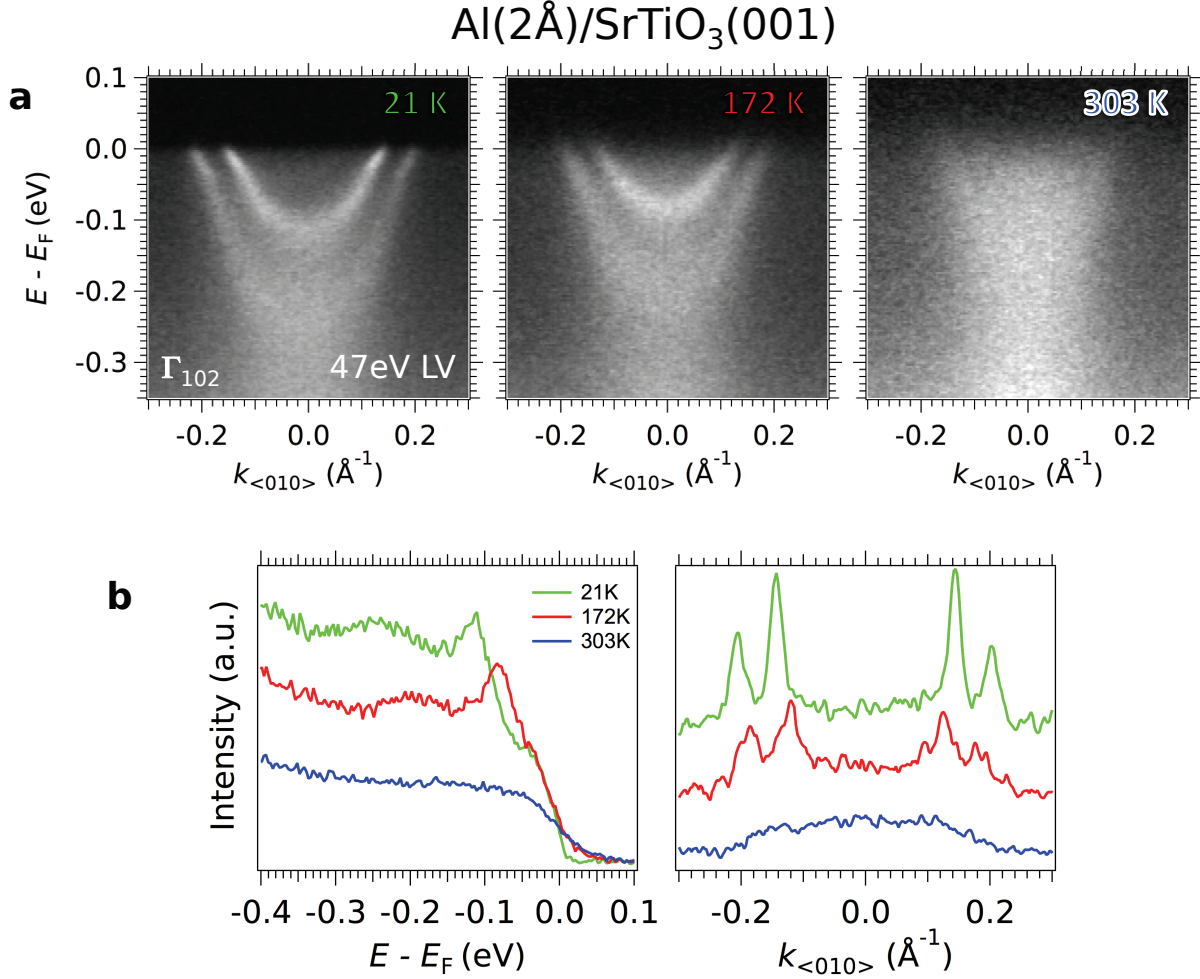


FIG. 5. (a) Energy-momentum map measured at the Al(2 Å)/SrTiO₃(001) interface prepared *in-situ* at different temperatures $T = 21$ K, 172 K and 303 K. Data were collected around the Γ_{102} point using LV photons at $h\nu = 47$ eV. (b) Energy and momentum distribution curves along $k_{<010>} = 0$ and the Fermi level of the $E - k$ maps in (a).

clearly visible at $T = 172$ K although the line widths are increased due to thermal broadening. At $T = 300$ K, the line widths are too large to identify the individual bands, although the left branch of the outer band is still visible close to the Fermi level E_F . Nevertheless, the spectral weight at the Fermi level demonstrates the existence and stability of the 2DES at room temperature. To compare the energy-momentum maps more directly, Figure 5(b) shows the energy distribution curves at $k_{<010>} = 0$ and the momentum distribution curves at Fermi level E_F . As can be seen from the value of the Fermi momenta k_F of the peaks in the MDCs as well as the binding energies of the peaks in the energy distribution curves (EDCs), the charge carrier density decreases slightly when temperature increases. We checked (not

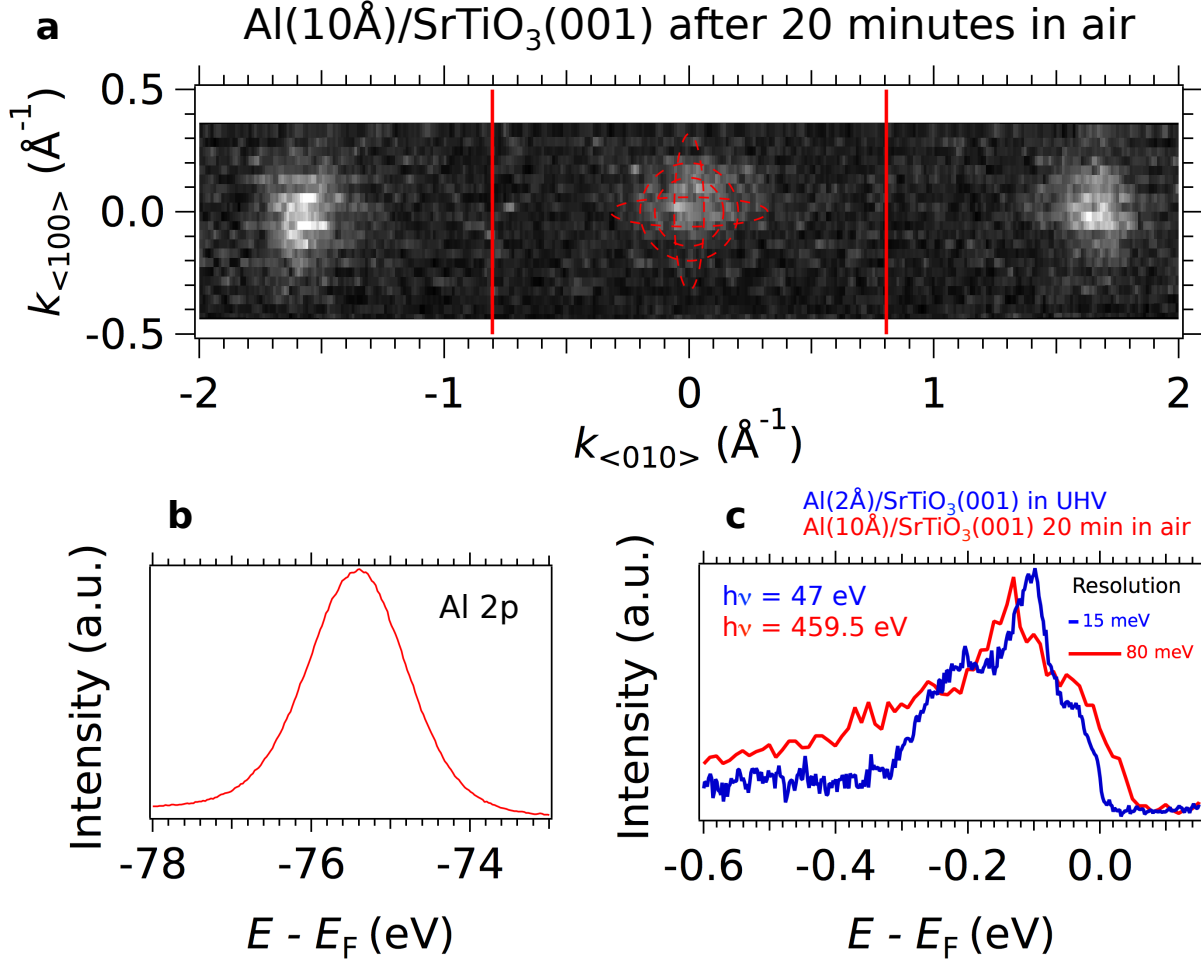


FIG. 6. (a) Fermi surface map measured in three neighboring Brillouin zones at $h\nu = 459.5$ eV on the Al(10Å)/SrTiO₃(001) interface prepared *in-situ* and subsequently exposed to air for $t = 20$ min. The red dashed circles and ellipses illustrate the Fermi surface shown in Figures 1(c, d) of the main text. The thick red lines correspond to the borders of the bulk Brillouin zones. (b) Angle-integrated spectrum of the Al 2p peak of the Al(10Å)/SrTiO₃(001) interface measured at $h\nu = 458.4$ eV. Due to the exposure to air, the Al film is completely oxidized –compare to Figure 2 of the main text. (c) Energy distribution curves integrated around Γ measured at the Al(10Å)/SrTiO₃(001) and Al(2Å)/SrTiO₃(001) interfaces. To facilitate the comparison, a momentum-independent background, due to spectral weight from the in-gap state, was removed from the EDC of the Al(2Å)/SrTiO₃(001) data.

shown) that these results are reproducible upon thermal cycling.

Effect of exposure to ambient conditions

In principle, the thicker the oxidized Al film the better the passivation of the surface against re-oxidation in ambient air pressure. For amorphous Al₂O₃ films grown by atomic

layer deposition on the surface of SrTiO₃(001), a film thickness of ≥ 1.2 nm is sufficient to create a stable 2DES at the Al₂O₃/SrTiO₃ interface [16]. Note that this value is identical to the thickness of the natural oxidized layer at the surface of aluminum (1.24 nm) [40]. Hence, this thickness is sufficient to prevent oxygen diffusion through a homogenous Al₂O₃ capping layer.

In our case, the probing depth of the high-resolution ARPES measurements, such as the ones shown in the main text, is limited by the mean free path of electrons which is ~ 5 Å at kinetic energies of $E_{kin} = 20 - 100$ eV. To increase the probing depth and probe the 2DES at buried interfaces, *e.g.* LaAlO₃/SrTiO₃, soft x-ray angle-resolved resonant photoelectron spectroscopy was applied previously [41]. Thus, to test the stability of the 2DES, we exposed an Al(10 Å)/SrTiO₃ sample to ambient conditions for about 30 minutes, and conducted soft x-ray resonant ARPES ($h\nu=459.5$ eV) at low temperatures. Note that 1 nm of Al corresponds to about 1.25 nm of Al₂O₃ which is close to the “critical” passivation thickness mentioned above.

As can be seen from the Fermi surface in **Figure 6(a)**, the 2DES at the Al(10 Å)/SrTiO₃ interface still exists after the exposure to air. For comparison, the red dashed circles and ellipses represent the Fermi surfaces measured at the ultra-thin Al(2 Å)/SrTiO₃ interface –see Figures 1(c, d) of the main text. Note that the 10 Å Al layer was completely oxidized after exposure to air, as demonstrated by the peak shape of the Al-2p peak in Figure 6(b). The data quality in these soft-X-ray ARPES measurements is lower compared to UV-measurements as the surface is not pristine anymore after exposure to air, the 2DES is buried below a thick oxidized Al film, the photoemission cross section of the valence states is much smaller at higher photon energies, and the total energy resolution at $h\nu = 459.5$ eV is about 80 meV, compared to 15 meV at $h\nu = 47$ eV. However, it is clear that the Fermi surface, and hence the charge-carrier density, are comparable between the Al(10Å)/SrTiO₃ sample exposed to air and the pristine Al(2Å)/SrTiO₃.

Figure 6(c) compares the momentum-integrated band structure around Γ for the two different interfaces, confirming that their electronic structures are comparable. Thus, these results demonstrate that the oxidized Al/SrTiO₃ interface effectively passivates the 2DES on SrTiO₃.

In order to adapt the method of creation of 2DES at the Al/oxide interface to transport measurements, and to be certain that the oxidized Al layer completely blocks oxygen

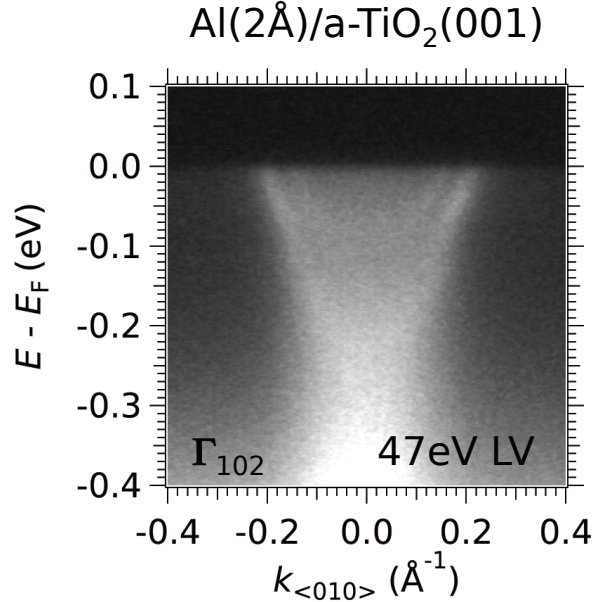


FIG. 7. Energy-momentum intensity map measured at the Al(2 Å)/a-TiO₂(001) interface prepared *in-situ*. The data was recorded at $T = 8$ K using LV photons at $h\nu = 47$ eV around the Γ_{102} point.

diffusion, a capping layer thickness above the “critical” passivation value of ~ 1.2 nm is necessary. At the same time, the capping layer suitable for transport should be insulating without contributions of metallic Al. Several possibilities should be explored in future studies: optimization of growth parameters (*e.g.* applying an oxygen partial pressure [40] during deposition after the first 2 Å of Al and/or a slight increase of the temperature to oxidize Al thicknesses greater than 2 Å) or deposition of another type of insulating capping layer after the deposition of 2 Å of Al.

Subband dispersions at the Al(2Å)/anatase interface

Figure 7 presents the ARPES energy-momentum intensity map at the Al(2Å)/a-TiO₂(001) interface. The two subbands form the circular Fermi surfaces shown in Figure 1(f) of the main text. As mentioned there, these Fermi surfaces are almost twice larger than their counterparts at the surface of anatase reduced by photons [26]. In agreement with this observation, the two subbands at the Al(2Å)/a-TiO₂(001) interface disperse down to larger binding energies: approximately -100 meV and -230 meV for the upper and lower subbands, respectively, while at the bare, reduced anatase surface they disperse only down

to about -60 meV and -170 meV [26].

Oxygen vacancy distribution at the Al(2Å)/anatase interface

The redox reaction creates oxygen vacancies at the Al(2Å)/oxide interface. The spatial distribution of these electron donors results in the creation of a potential well confining the electrons and forming the 2DES. To determine the distribution of vacancies, we measured the Ti-2*p* and Ti-3*p* core levels of anatase (001) using X-ray photoemission at $h\nu = 1150$ eV as a function of the electron emission angle, and at normal emission as a function of the X-ray photon energy, and fitted the peaks using either Voigt or Lorentzian line shapes together with a Shirley background. As can be seen in **Figures S8(a, b)**, the core levels are composed of several peaks (red markers) corresponding to Ti ions of different oxidation state (4+, 3+, and 2+) due to the presence of oxygen vacancies. We observe that the fraction of Ti-4⁺ of stoichiometric, insulating TiO₂ increases for larger electron escape depths, as evidenced by the angle and photon energy dependencies in Figures S8(a, b). By contrast, the Ti-3⁺ and Ti-2⁺ components, associated to free carriers and oxygen vacancies, become increasingly important for smaller escape depths and thus, closer to the interface.

To obtain the concentration profile $c(z, Ti^{x+})$ of the Ti^{x+} species along the confinement direction z perpendicular to the surface, we calculate the total area of the corresponding core level peak by:

$$a(Ti) \propto \int dz \sum_{x=2,3,4} c(z, Ti^{x+}) \exp\left(-\frac{d(z)}{\lambda(E_{kin})}\right),$$

where $d(z)$ is the distance travelled by a photo-emitted electron inside matter (*i.e.*, anatase + AlO_x layer), which depends on the emission angle, and λ the inelastic mean free path for electrons photo-emitted with kinetic energy E_{kin} .

Figure 8(c) shows the ratio $[a(Ti^{2+}) + a(Ti^{3+})]/a(Ti^{4+})$ as a function of the electron emission angle. The error bars indicate the variation of this ratio using different line shapes and backgrounds to fit the various Ti peaks. We then fit the observed changes in such peak area ratio using a Heavyside function for the concentration profile of oxygen vacancies, as shown in Figure 8(d). The result of the fit, shown by the dashed curve in Figure 8(c), yields a depth of 9 ± 3 Å for the vacancy-rich layer below the surface, and a fraction of $(62 \pm 15)\%$

Al(2Å)/a-TiO₂(001)

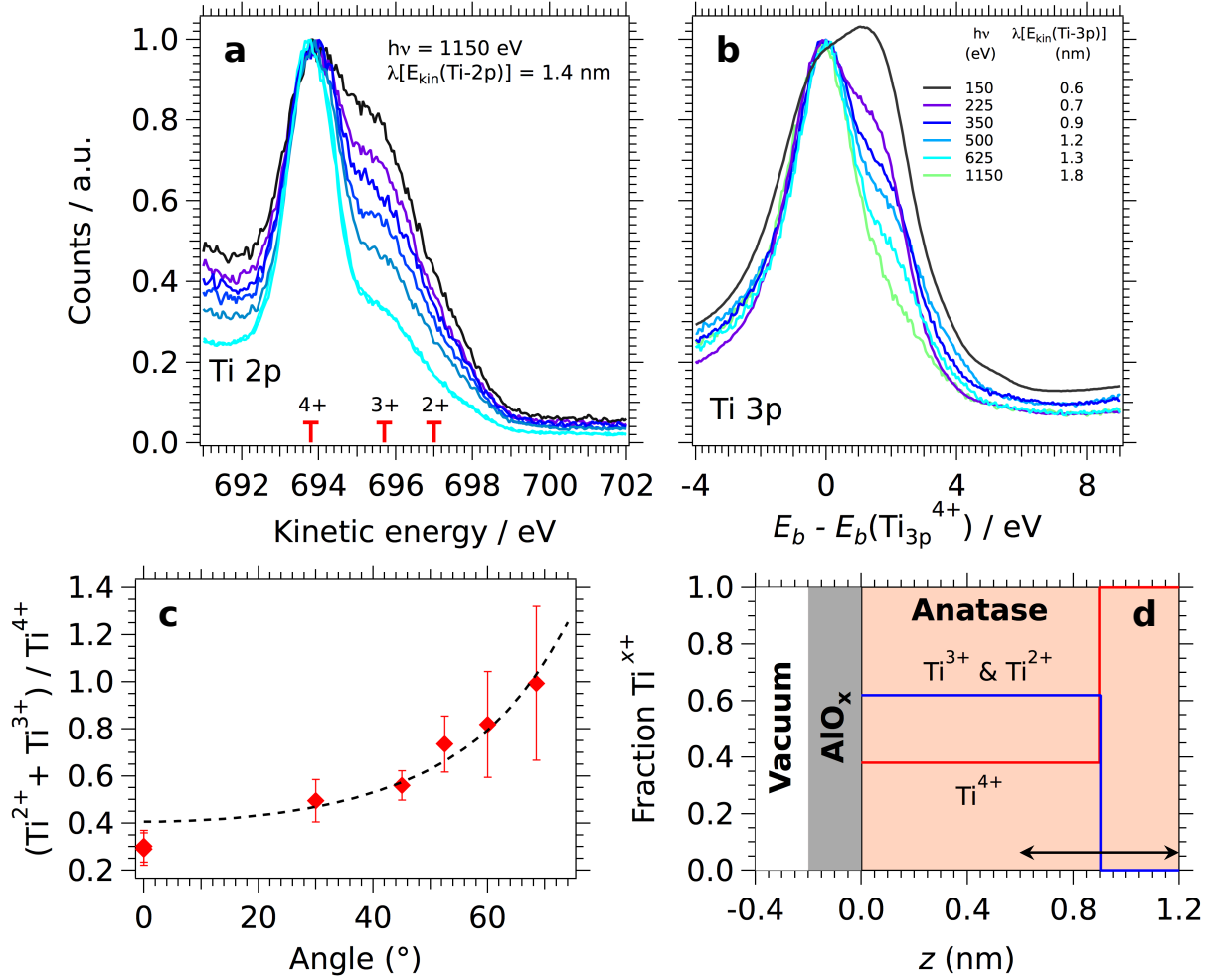


FIG. 8. (a) XPS at the Ti-2*p* core level of Al(2Å)/a-TiO₂ (001) as a function of emission angle using $h\nu = 1150$ eV photons. At this photon energy, the universal inelastic mean free path of electrons emitted from the Ti-2*p* peak is $\lambda[E_{kin}(\text{Ti-2}p)] = 1.4$ nm [42]. The red markers and corresponding error bars indicate the peak positions and uncertainties for the different Ti oxidation state (4+, 3+, and 2+). (b) XPS at the Ti-3*p* core level of anatase (001) at normal emission as a function of photon energy. The inelastic mean free path of electrons emitted from the Ti-3*p* peak at different photon energies is specified in the inset table. The XPS intensity in panels (a) and (b) is normalized to the Ti⁴⁺ peak. (c) Ratio of intensities, from panel (a), between the Ti²⁺ + Ti³⁺ shoulder and the Ti⁴⁺ peak as a function of the electron ejection angle. The dashed curve is the best fit to the data assuming a step-like distribution of vacancies over 9 ± 3 Å below the surface, as schematized in panel (d). (d) Model used for the distribution of the different Ti oxidation states due to oxygen vacancies beneath the AlO_x/anatase interface: blue line for Ti²⁺ + Ti³⁺, red line for Ti⁴⁺. The double arrow indicates the error bar in the determination of the vacancy depth distribution.

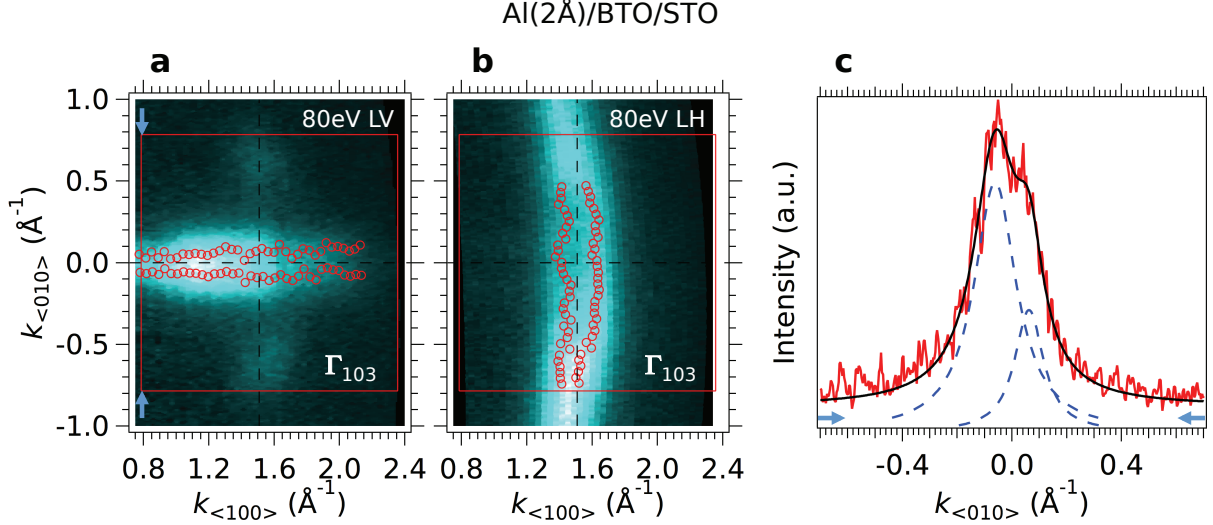


FIG. 9. (a, b) Fermi surface maps (spectral weight integrated over $E_F \pm 5$ meV) at the the Al(2Å)/BaTiO₃ interface using 80 eV LV and LH photons, respectively. Data were collected around the Γ_{103} Brillouin zone. The open red circles show the Fermi momenta obtained from Lorentzian fits to the MDCs at E_F . The red squares show the Brillouin-zone edges. (c) MDC integrated over $E_F \pm 10$ meV along the left edge of the Γ_{103} Brillouin zone, corresponding to a cut along the light blue arrows in panel (a). The blue dashed curves are Lorentzian peaks, and the black curve is the resulting total fit.

of Ti ions with oxidation states 3+ or 2+.

In-plane and out-of-plane Fermi surfaces of the 2DES in BaTiO₃

Figures S9(a, b) show the Fermi-surface strips formed by the heavy bands of the 2DES at the surface of BaTiO₃ (Al(2Å)/BTO/Nb:STO interface). The data were taken on the same Brillouin zone using mutually orthogonal photon polarizations, which due to photoemission selection rules enhance either the Fermi strip parallel to $k_{<010>}$ or the Fermi strip parallel to $k_{<100>}$. The open red circles show the Fermi momenta obtained from Lorentzian fits to the MDCs at E_F . Figure 9(c) shows one of such MDCs, corresponding to a cut at the left edge of the Γ_{103} Brillouin zone (light blue arrows). This MDC clearly shows a double-peak structure, corresponding to the two Fermi sheets of the Fermi strip, which is thus open at the Brillouin-zone edge. This is in agreement with the fact that the heavy bands running along the $k_{<010>}$ and $k_{<010>}$ directions do not cross E_F , as shown in Figures 3(d, e) of the main text. From these MDC fits, the average distance between opposite Fermi momenta along the short side of the Fermi strips is $k_s \approx 0.15 \pm 0.02$ Å⁻¹.

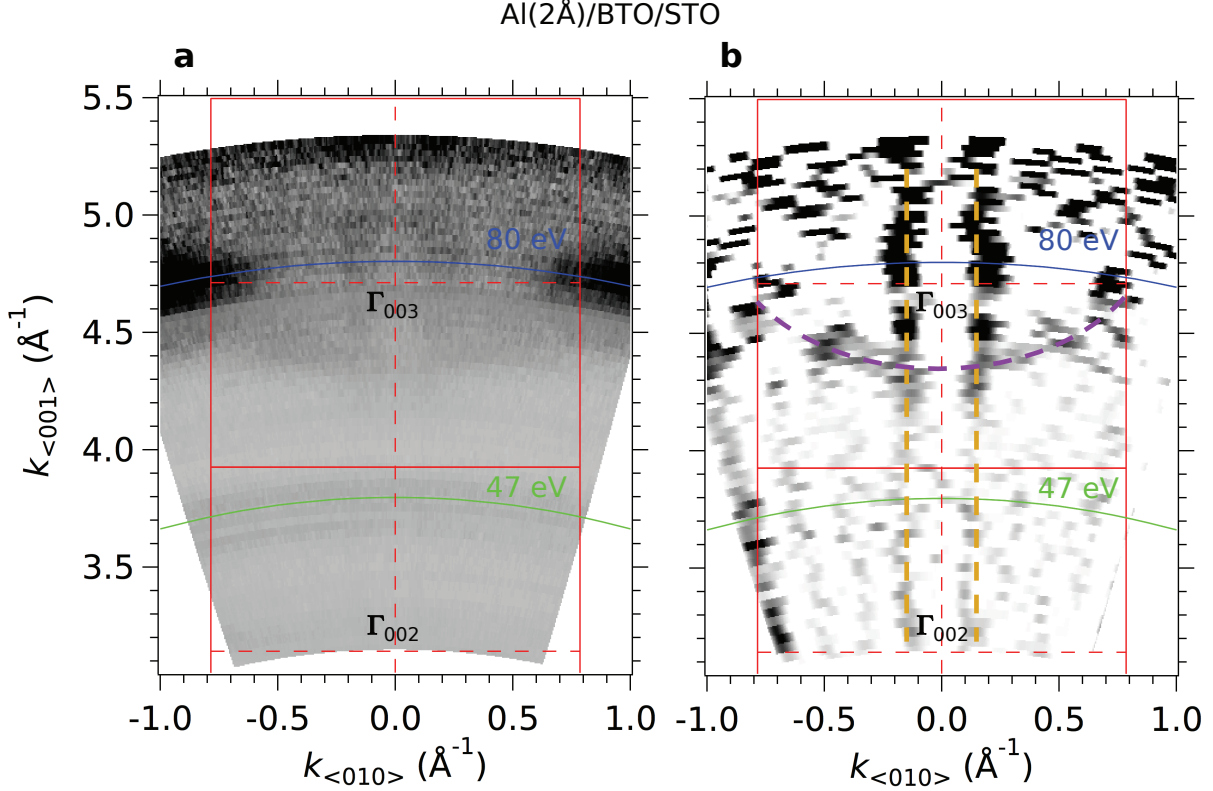


FIG. 10. (a) Raw Fermi surface map at the the Al(2Å)/BaTiO₃ interface in the $k_{\langle 001 \rangle} - k_{\langle 010 \rangle}$ plane, acquired by varying the photon energy in 1 eV steps between $h\nu_1 = 30$ eV and $h\nu_2 = 100$ eV using LH photons. To calculate the momentum perpendicular to the surface, we use a free-electron final-state approximation, and set the inner potential to $V_0 = 12$ eV. The spectral weight was integrated over $[E_F - 30, E_F + 5]$ meV. The red square shows the edges of the Γ_{003} bulk Brillouin zone. The blue and green arcs show the spherical-cap cuts in 3D reciprocal space obtained with $h\nu = 80$ eV and $h\nu = 47$ eV, respectively, corresponding to the data presented in Figure 3 of the main text. (b) Second derivative (negative values only) of the Fermi surface map in (a). The yellow and purple dashed curves are guides to the eye showing, respectively, the non-dispersive Fermi surface of the light d_{xy} -like states, and the dispersive Fermi surface of the heavy $d_{xz/yz}$ -like states.

Finally, **Figures S10(a, b)** show the out-of-plane Fermi-surface map of the 2DES at the surface of BaTiO₃, obtained from the photon-energy dependence of the electronic structure measured over more than an entire bulk Brillouin zone. The inner cylinder, yellow dashed lines in Figure 10(b), is associated to the light d_{xy} -like band forming the Fermi circle in the plane. As its Fermi surface does not disperse along the confinement direction, it corresponds to a 2D-like state. The data also show a large ellipse dispersing along $k_{\langle 001 \rangle}$, hence presenting a 3D-like character, best seen in the lower part of the Γ_{003} Brillouin zone, purple dashed lines in Figure 10(b). This Fermi sheet is associated to the heavy bands forming

the Fermi strips in the plane. Of course, such 3D-like behavior cannot correspond to a true bulk state, as the redox reaction occurs only at the interface region. Note also that the 3D carrier density resulting from such a state would be huge, comparable to that of good metals, while the bulk BTO film is still insulating. Instead, such 2D-3D dichotomy between different states forming the 2DES in BaTiO₃, also observed for the 2DES at the surface of SrTiO₃ [31], can be qualitatively understood as arising from confinement itself. In the bulk, by cubic symmetry, the t_{2g} bands are expected to form 3 identical mutually orthogonal Fermi surfaces similar to prolate ellipsoids along the main crystallographic axes –or open quasi-cylinders, when the band filling is such that the ellipsoids’ long axis extends beyond the zone boundary. Confinement along z will result, by Heisenberg’s principle, in “de-confinement”, or elongation, of the ellipsoids along k_z . When the confinement length becomes $\lesssim a$ (one unit cell), the ellipsoid stretches over $k_z \gtrsim 2\pi/a$ (one Brillouin zone), and the out-of-plane Fermi surface becomes a cylinder.

Thus, in the case of the 2DES at the surface of BaTiO₃, we see from Figure 9 that the Fermi-surface strip formed by $d_{xz/yz}$ -like states has an in-plane Fermi momentum $k_F = k_s/2 = 0.075 \text{ \AA}^{-1}$, while from Figure 10 its out-of-plane Fermi momentum is approximately 0.4 \AA^{-1} . Hence, there is an elongation along k_z of the $d_{xz/yz}$ ellipsoids due to confinement. Similarly, as noted before, the in-plane circular Fermi surface, formed by d_{xy} -like states, forms a cylinder along the out-of-plane direction. We then conclude that the planar d_{xy} -like states are more tightly confined to the surface, while the non-planar $d_{xz/yz}$ -like states extend over multiple unit cells towards the bulk. This situation is wholly similar to the case of the 2DES at the surface of SrTiO₃ [31], and simply reflects the fact that the confinement potential is wedge-shaped, such that electrons with a large effective mass along k_z (d_{xy} states) are more confined than electrons with a small effective mass along k_z ($d_{xz/yz}$ states) [19, 31].

* andres.santander-syro@universite-paris-saclay.fr

- [1] A. Ohtomo, H.Y. Hwang, *Nature* **2004**, 427, 423.
- [2] S. Thiel, G. Hammerl, A. Schmehl, C.W. Schneider, J. Mannhart, *Science* **2006**, 313, 1942.
- [3] N. Reyren, S. Thiel, A.D. Caviglia, L. Fitting Kourkoutis, G. Hammerl, C. Richter, C.W. Schneider, T. Kopp, A.-S. Rüetschi, D. Jaccard, M. Gabay, D.A. Muller, J.-M. Triscone, J.

- Mannhart, *Science* **2007**, *317*, 1196.
- [4] A.D. Caviglia, S. Gariglio, N. Reyren, D. Jaccard, T. Schneider, M. Gabay, S. Thiel, G. Hammerl, J. Mannhart, J.-M. Triscone, *Nature* **2008**, *456*, 642.
- [5] A. Brinkman, M. Huijben, M. van Zalk, J. Huijben, U. Zeitler, J.C. Maan, W.G. van der Wiel, G. Rijnders, D.H.A. Blank, H. Hilgenkamp, *Nature Mater.* **2007**, *6*, 493.
- [6] L. Li, C. Richter, J. Mannhart, R.C. Ashoori, *Nature Phys.* **2011**, *7*, 762.
- [7] J.A. Bert, B. Kalisky, C. Bell, M. Kim, Y. Hikita, H.Y. Hwang, K.A. Moler, *Nature Phys.* **2011**, *7*, 767.
- [8] A.D. Caviglia, M. Gabay, S. Gariglio, N. Reyren, C. Cancellieri, J.M. Triscone, *Phys. Rev. Lett.* **2010**, *104*, 126803.
- [9] M. Ben Shalom, A. Ron, A. Palevski, Y. Dagan, *Phys. Rev. Lett.* **2010**, *105*, 206401.
- [10] Santander-Syro, A.F. *et al.* A.F. Santander-Syro, F. Fortuna, C. Bareille, T.C. Rödel, G. Landolt, N.C. Plumb, J.H. Dil, M. Radovic, *Nat. Mater.* **2014**, *13*, 1085.
- [11] H. Takagi, H. Y. Hwang, *Science* **2010**, *327*, 1601.
- [12] J. Mannhart, D.G. Schlom, *Science* **2010**, *327*, 1607.
- [13] H.Y. Hwang, Y. Iwasa, M. Kawasaki, B. Keimer, N. Nagaosa, Y. Tokura, *Nature Mater.* **2012**, *11*, 103.
- [14] N. Nakagawa, H.Y. Hwang, D.A. Muller, *Nature Mater.* **2006**, *5*, 204.
- [15] Y.Z. Chen, N. Pryds, J.E. Kleibecker, G. Koster, J. Sun, E. Stamate, B. Shen, G. Rijnders, S. Linderoth, *Nano letters* **2011** *11*, 3774.
- [16] S.W. Lee, Y. Liu, J. Heo, R.G. Gordon, *Nano letters* **2012**, *12*, 4775.
- [17] J. Delahaye, T. Grenet, *Journal of Physics D: Applied Physics* **2012**, *45*, 315301.
- [18] E. Lesne *et al.* , *Nat. Commun.* **2014**, *5*, 4291.
- [19] A.F. Santander-Syro, O. Copie, T. Kondo, F. Fortuna, S. Pailhes, R. Weht, X.G. Qiu, F. Bertran, A. Nicolaou, A. Taleb-Ibrahimi, P. Le Fèvre, G. Herranz, M. Bibes, N. Reyren, Y. Apertet, P. Lecoeur, A. Barthélémy, M.J. Rozenberg, *Nature* **2011**, *469*, 189.
- [20] W. Meevasana, P.D.C. King, R.H. He, S.-K. Mo, M. Hashimoto, A. Tamai, P. Songsiriritthigul, F. Baumberger, Z.-X. Shen, *Nature Mater.* **2011**, *10*, 114.
- [21] A.F. Santander-Syro, C. Bareille, F. Fortuna, O. Copie, M. Gabay, F. Bertran, A. Taleb-Ibrahimi, P. Le Fèvre, G. Herranz, N. Reyren, M. Bibes, A. Barthélémy, P. Lecoeur, J. Guevara, M.J. Rozenberg, *Phys. Rev. B* **2012**, *86*, 121107.

- [22] P.D.C. King, R.H. He, T. Eknapakul, P. Buaphet, S.-K. Mo, Y. Kaneko, S. Harashima, Y. Hikita, M.S. Bahramy, C. Bell, Z. Hussain, Y. Tokura, Z.-X. Shen, H.Y. Hwang, F. Baumberger, W. Meevasana, *Phys. Rev. Lett.* **2012**, *108*, 117602.
- [23] C. Bareille, F. Fortuna, T.C. Rödel, F. Bertran, M. Gabay, O. Hijano Cubelos, A. Taleb-Ibrahimi, P. Le Fèvre, M. Bibes, A. Barthélémy, T. Maroutian, P. Lecoeur, M.J. Rozenberg, A.F. Santander-Syro, *Scientific Reports* **2014**, *4*, 1.
- [24] T.C. Rödel, C. Bareille, F. Fortuna, C. Baumier, F. Bertran, P. Le Fèvre, M. Gabay, O. Hijano Cubelos, M.J. Rozenberg, T. Maroutian, P. Lecoeur, A.F. Santander-Syro, *Phys. Rev. Applied* **2014**, *1*, 051002.
- [25] S. McKeown Walker, A. de la Torre, F.Y. Bruno, A. Tamai, T.K. Kim, M. Hoesch, M. Shi, M.S. Bahramy, F. Baumberger, *Phys. Rev. Lett.* **2014**, *113*, 177601.
- [26] T.C. Rödel, F. Fortuna, F. Bertran, M. Gabay, M.J. Rozenberg, A.F. Santander-Syro, P. Le Fèvre, *Phys. Rev. B* **2015**, *92*, 041106(R).
- [27] Q. Fu, T. Wagner, *Surface Science Reports* **2007** *62*, 431.
- [28] Q. Fu, T. Wagner, *The Journal of Physical Chemistry B* **2005**, *3*, 11697.
- [29] S.-I. Kim, D.-H. Kim, Y. Kim, S.Y. Moon, M.-G. Kang, J.K. Choi, H.W. Jang, S.K. Kim, J.-W. Choi, S.-J. Yoon, H.J. Chang, C.-Y. Kang, S. Lee, S.-H. Hong, J.-S. Kim, S.-H. Baek, *Adv. Mater.* **2013**, *25*, 4612.
- [30] V.T. Tra, J.-W. Chen, P.-C. Huang, B.-C. Huang, Y. Cao, C.-H. Yeh, H.-J. Liu, E.A. Eliseev, A.N. Morozovska, J.-Y. Lin, Y.-C. Chen, M.-W. Chu, P.-W. Chiu, Y.-P. Chiu, L.-Q. Chen, C.-L. Wu, Y.-H. Chu, *Adv. Mater.* **2013**, *25*, 3357.
- [31] N.C. Plumb, M. Salluzzo, E. Razzoli, M. Månsson, M. Falub, J. Krempasky, C.E. Matt, J. Chang, M. Schulte, J. Braun, H. Ebert, J. Minár, B. Delley, K.-J. Zhou, T. Schmitt, M. Shi, J. Mesot, L. Patthey, M. Radovic, *Phys. Rev. Lett.* **2014** *113*, 086801.
- [32] P.D.C. King, S. McKeown Walker, A. Tamai, A. de la Torre, T. Eknapakul, P. Buaphet, S.-K. Mo, W. Meevasana, M.S. Bahramy, F. Baumberger, *Nature communications* **2014**, *5*, 3414.
- [33] A. Schilling, T.B. Adams, R.M. Bowman, J.M. Gregg, G. Catalan, J.F. Scott, *Phys. Rev. B* **2006**, *74*, 024115.
- [34] N.A. Pertsev, A.G. Zembilgotov, A.K. Tagantsev, *Phys. Rev. Lett.* **1998**, *80*, 1988.
- [35] K.J. Choi, M. Biegalski, Y.L. Li, A. Sharan, J. Schubert, R. Uecker, P. Reiche, Y.B. Chen, X.Q. Pan, V. Gopalan, L.-Q. Chen, D.G. Schlom, C.B. Eom, K.J. Choi, *Science* **2004**, *306*,

1005.

- [36] J. Chen, Y. Luo, X. Ou, G. Yuan, Y. Wang, Y. Yang, J. Yin, Z. Liu, *J. Appl. Phys.* **2013**, *113*, 204105.
- [37] S. Goswami, E. Mulazimoglu, L.M.K. Vandersypen, A.D. Caviglia, *Nano Lett.* **2015**, *15*, 2627.
- [38] M. Setvín, B. Daniel, V. Mansfeldova, L. Kavan, P. Scheiber, M. Fidler, M. Schmid, U. Diebold, *Surface Science*, **2014**, *626*, 61.
- [39] N.P. Guisinger, T.S. Santos, J.R. Guest, T.-Y. Chien, A. Bhattacharya, J.W. Freeland, M. Bode, *ACS nano*, **2009**, *3*, 4132.
- [40] N. Cai, G. Zhou, K. Müller, D.E. Starr *Phys. Rev. Lett.*, **2011**, *107*, 035502.
- [41] G. Berner, M. Sing, H. Fujiwara, A. Yasui, Y. Saitoh, A. Yamasaki, Y. Nishitani, A. Sekiyama, N. Pavlenko, T. Kopp, C. Richter, J. Mannhart, S. Suga, R. Claessen, *Phys. Rev. Lett.*, **2013**, *110*, 247601.
- [42] M. P. Seah and W. A. Dench, *Surface and Interface Analysis*, **1979**, *1*, 2.